Systems/Circuits

Distributed and Localized Dynamics Emerge in the Mouse Neocortex during Reach-to-Grasp Behavior

Eros Quarta,[1,2*] Alessandro Scaglione,[1,2*] Jessica Lucchesi,[2] Leonardo Sacconi,[2,3] Anna Letizia Allegra Mascaro,[2,4#] and Francesco Saverio Pavone[1,2,3#]

[1]Department of Physics and Astronomy, University of Florence, Sesto Fiorentino, Florence, 50019, Italy, [2]European Laboratory for Non-Linear Spectroscopy, Sesto Fiorentino, Florence, 50019, Italy, [3]National Instute of Optics, National Research Council, Sesto Fiorentino, Florence, 50019, Italy, and [4]Neuroscience Institute, National Research Council, Pisa, 56124, Italy

A long-standing question in systems neuroscience is to what extent task-relevant features of neocortical processing are localized or distributed. Coordinated activity across the neocortex has been recently shown to drive complex behavior in the mouse, while activity in selected areas is canonically associated with specific functions (e.g., movements in the case of the motor cortex). Reach-to-grasp (RtG) movements are known to be dependent on motor circuits of the neocortex; however, the global activity of the neocortex during these movements has been largely unexplored in the mouse. Here, we characterized, using wide-field calcium imaging, these neocortex-wide dynamics in mice of either sex engaging in an RtG task. We demonstrate that, beyond motor regions, several areas, such as the visual and the retrosplenial cortices, also increase their activity levels during successful RtGs, and homologous regions across the ipsilateral hemisphere are also involved. Functional connectivity among neocortical areas increases transiently around movement onset and decreases during movement. Despite this global phenomenon, neural activity levels correlate with kinematics measures of successful RtGs in sensorimotor areas only. Our findings establish that distributed and localized neocortical dynamics co-orchestrate efficient control of complex movements.

Key words: **calcium imaging; functional connectivity; neocortex; neural dynamics; reach-to-grasp; voluntary movement**

Significance Statement

Mammals rely on reaching and grasping movements for fine-scale interactions with the physical world. In the mouse, the motor cortex is critical for the execution of such behavior, yet little is known about the activity patterns across neocortical areas. Using the mesoscale-level networks as a model of cortical processing, we investigated the hypothesis that areas beyond the motor regions could participate in RtG planning and execution, and indeed a large network of areas is involved while performing RtGs. Movement kinematics correlates mostly with neural activity in sensorimotor areas. By demonstrating that distributed and localized neocortical dynamics for the execution of fine movements coexist in the mouse neocortex during RtG, we offer an unprecedented view on the neocortical correlates of mammalian motor control.

Introduction

Deciphering how the CNS produces goal-directed movements, such as the reach-to-grasp (RtG), is crucial for expanding our understanding of the neural computations underlying motor ability and animal cognition in general (Bayne et al., 2019). RtG is known to be dependent on neocortical circuits, and intensive research has provided detailed insight into how neural activity from motor areas of the neocortex contributes to the control of movements (Evarts, 1968; Georgopoulos et al., 1982; Graziano et al., 2002; Churchland et al., 2012). In rodents, medial prefrontal regions, such as the secondary motor cortex (also termed medial agranular cortex, precentral cortex, or frontal orienting field), have been shown to be critical for movement preparation (N. Li et al., 2016; Barthas and Kwan, 2017; Chen et al., 2017). Nevertheless, how neural systems give rise to behavior cannot be fully comprehended from segregated analysis of its components. Indeed, parallel to the patterns of neural activity at the local level, information processing occurring at the corticocortical level is

Received Apr. 6, 2020; revised May 25, 2021; accepted Aug. 18, 2021.

Author contributions: E.Q., L.S., A.L.A.M., and F.S.P. designed research; E.Q., A.S., J.L., L.S., and A.L.A.M. performed research; E.Q., A.S., J.L., and A.L.A.M. analyzed data; E.Q. wrote the first draft of the paper; E.Q., A.S., J.L., L.S., A.L.A.M., and F.S.P. edited the paper; E.Q. and A.S. wrote the paper.

This work was supported by European Union's Horizon 2020 Research and Innovation Program Grant Agreement 785907 (HBP SGA2); Italian Ministry for Education, University, and Research (Project FARE MIMIC); and European Research Council (European Union's Horizon 2020 Research and Innovation Program Grant Agreement 692943). We thank the staff of the mechanical and electronic workshops of European Laboratory for Non-Linear Spectroscopy for assistance; members of the F.S.P. laboratory for helpful discussions and suggestions; Costanza Campaioli and Chiara Caldini for help in developing earlier versions of the experimental setup; and Prof. Matteo Caleo for useful comments on the manuscript.

*E.Q. and A.S. contributed equally to this work as co-first authors.

#A.L.A.M. and F.S.P. contributed equally to this work as co-last authors.

The authors declare no competing financial interests.

E. Quarta's present address: Department of Physiology and Pharmacology, Sapienza University of Rome, Piazzale Aldo Moro, 5, Rome, 00185, Italy.

Correspondence should be addressed to Francesco Saverio Pavone at pavone@lens.unifi.it.

https://doi.org/10.1523/JNEUROSCI.0762-20.2021

Copyright © 2022 the authors

necessary for complex behavior (Peters et al., 2014; Allen et al., 2017; Battaglia-Mayer and Caminiti, 2019).

However, despite the growing adoption of the mouse for elucidating the neural underpinnings of motor control (Ölveczky, 2011), the neocortex-wide dynamics during RtG remain largely unexplored. Advancements in optical methods, especially wide-field fluorescence microscopy, have allowed monitoring neuronal activity from almost the entire dorsal neocortex in awake, behaving mice (Allegra Mascaro et al., 2019; Montagni et al., 2019; Sancataldo et al., 2019; Ren and Komiyama, 2021). With this tool, it has been recently shown that neocortex-wide dynamics emerge during learning (Makino et al., 2017); nevertheless, the contribution of regions beyond the contralateral motor areas and the corticocortical interactions during skilled movements remain largely unexplored. Also, while movement kinematics are associated with neural activity in the contralateral motor areas, and information about such activity can also be used to predict several features of the executed movement (Prsa et al., 2017; C. Li et al., 2019), information on the relationship between RtG kinematics and neural activity across the neocortex is still scanty.

Our results indicate that global cortical activation emerges during successful RtGs, with functional connectivity (FC) across areas peaking around movement onset, whereas movement kinematics correlated only with the activity in a portion of the sensorimotor region.

Materials and Methods

Transgenic mice

All experimental procedures were authorized by the Italian Ministry of Health (authorization 127-2018-PR). A total of 9 mice (3-11 months of age) were used in this study. Six (3 male, 3 female) were GCaMP mice (C57BL/6J-Tg(Thy1-*GCaMP6f*)GP5.17Dkim/J, stock #025393, herein referred to as *GCaMP6f*) (Chen et al., 2013), whereas 3 (2 females, 1 male) *GFP* mice (Tg(Thy1-EGFP)MJrs, stock #007788) were used as controls to account for potential hemodynamic artifacts. Animals were housed on a 12 h light/dark cycle with *ad libitum* water. Mice undergoing behavioral training were food-restricted to 80%-90% of original body weight by limiting food intake to 2-3 g/d. Animals were monitored and weighed daily, and food ratios were increased if necessary. Veterinary staff monitored animals twice a week.

Surgery

The day before surgery, mice were given a subcutaneous injection of enrofloxacin (10 mg/kg) and each day thereafter for 3 d, to prevent infections. On the day of surgery, animals were anesthetized with isoflurane (3% induction, 1.5% maintenance) and placed on a stereotaxic apparatus (Kopf Instruments). The absence of tail reflex and toe-pinch reflex was tested to confirm that the mouse was adequately anesthetized. Throughout the surgery, the temperature was kept constant at 37°C by means of an electric heating pad controlled by a rectal temperature sensor (Stoelting). To prevent cornea dehydration, ophthalmic gel was applied over the eyes. The scalp was first scrubbed with ethanol and betadine, then a depilatory cream was applied to remove hairs, and then a few drops of a topic agent (lidocaine hydrochloride 2%) were applied as an analgesic measure. A circular piece of scalp was removed, and the anatomic points of reference (bregma and λ) were stained with a permanent marker. Two semicircular coverslip glasses, one per hemisphere, were glued on the skull above the cortex using a transparent dental cement. A custom-built headpost was placed ~0.5 mm posterior to λ. At the end of the surgery, subcutaneous injections of analgesic and anti-inflammatory (carprofen, 5 mg/kg) drugs were given to facilitate recovery. To this end, 200 ml lactated Ringer's solution of the 0.9% saline was given to each mouse at the end of surgery. Mice were allowed to recover at least 1 week following surgery. During this period, animals were given *ad libitum* food and water.

Behavioral apparatus

The experimental apparatus (see Fig. 1*A*) comprised a stage (size 300 × 300 × 20 mm, Thorlabs) and walls to form an enclosure and secured above a lab jack (MLJ050/M, Thorlabs) and was inspired by the work of Guo et al. (2015). The enclosure is equipped with a base for the animal, a perch, a speaker to deliver the auditory cue, and a turntable attached to a servo-motor equipped with a contactless magnetic rotary encoder to ensure consistent pellet positioning (MX-28AT) and controlled by a controller board (ArbotiX-M. Robocontroller, Trousser Robotics). The servo is controlled via an ad hoc program. Chocolate pellets (10 mg, 5TUL Purified 10 mg pellets, catalog 1811529, TestDiet) were used to induce the RtG movements, thus serving as stimuli. The interstimulus interval was 6-20 s. The enclosure was placed within a custom-made sensory-isolated enclosed imaging recording chamber that is kept dark and has been insulated with acoustic foam to further reduce ambient sounds (RS components and woods).

The behavioral data were collected at 200 frames/s via a high-speed camera (CM3-U3-13YC-CS, Chameleon3, FLIR) with 2.8-8 mm varifocal objective lenses (LENS-30F2-V80CS, Fujinon), placed to the left of the head-fixed animal. A 470 nm LED illuminating the stage was used as light source to create a high-contrast image for processing and quantification. Movies were recorded using the FlyCapture software (FLIR).

Wide-field microscopy

Imaging was performed through the intact skull using a custom-made microscope. The microscope consisted of back-to-back 50 mm f/1.2 camera lenses (Nikon), separated by a FF495-Di03-50.8-D dichroic mirror (Semrock), mounted in a 60 mm cube (Thorlabs). To excite the *GCaMP6f* indicator, a 470 nm light source (LED, M470L3, Thorlabs) was deflected by a dichroic filter (DC FF 495-DI02 Semrock) on the objective (TL2X-SAP 2× Super Apochromatic Microscope Objective, 0.1 NA, 56.3 mm WD, Thorlabs). The fluorescence signal was selected by a bandpass filter (525/50 Semrock) and collected by a CMOS camera (ORCA-Flash 4.0 V2, Hamamatsu). Images were acquired at 25 Hz, with a resolution of 512 × 512 pixels with a FOV of ~12 × 12 mm (depth 16-bit) via the HCImage Live software (Hamamatsu). The microscope thus allows a FOV embracing the entire dorsal prospect of the mouse neocortex. To reduce unwanted light scattering on the mouse eyes (which could serve as visual stimuli, inducing unwanted neural activity), an iris (ID15/M, Mounted Standard Iris, Ø15 mm Max Aperture, TR75/M. Post, Thorlabs) was placed 1-2 mm above the mouse skull. Imaging sessions were performed for each behavioral training session. The synchronization of the components of the experimental setup occurred via a common hardware trigger signal at the start of each block (for the definition, see Experimental design).

Experimental design. Following recovery from surgery for at least 1 week, mice were habituated to the experimental setup for ≥4 d (≥30 min a day/mouse). Then, mice were gently placed under the microscope objective and fixed (see Fig. 1*B*). Each session contained at least 5 blocks, and each block lasted between 65 s and 6 min, 50 s. Here, we analyzed the first 10 d starting from when the mouse performed the first successful RtG. The neural dynamics associated with both successful movements and with errors trials were analyzed. Successful RtGs attempts were defined as RtGs that ended with the pellet eaten, error RtGs attempts were defined as RtGs with reach that did not end with the pellet eaten because the animal missed the pellet or failed the grasp or dropped the pellet before eating it. We analyzed the neural dynamics for a total of 298 movements (n successful RtGs = 78, n error RtGs = 117, n successful RtGs performed by *GFP* mice = 103). To ensure consistency, only trajectories from successful RtG performed by GCaMP mice were analyzed.

Image processing and data analysis. For the movement data, image sequences were loaded onto FIJI (ImageJ) and the metacarpus position was tracked using the manual tracking plugin, to obtain the XY coordinates of the RtGs. The timing of the movement onset (MoveON) was defined as the frame for which the operator detected a variation in the metacarpus position. The metacarpi coordinates were then used to reconstruct the movement trajectories and compute the movement kinematics. We computed the following kinematics parameters that were

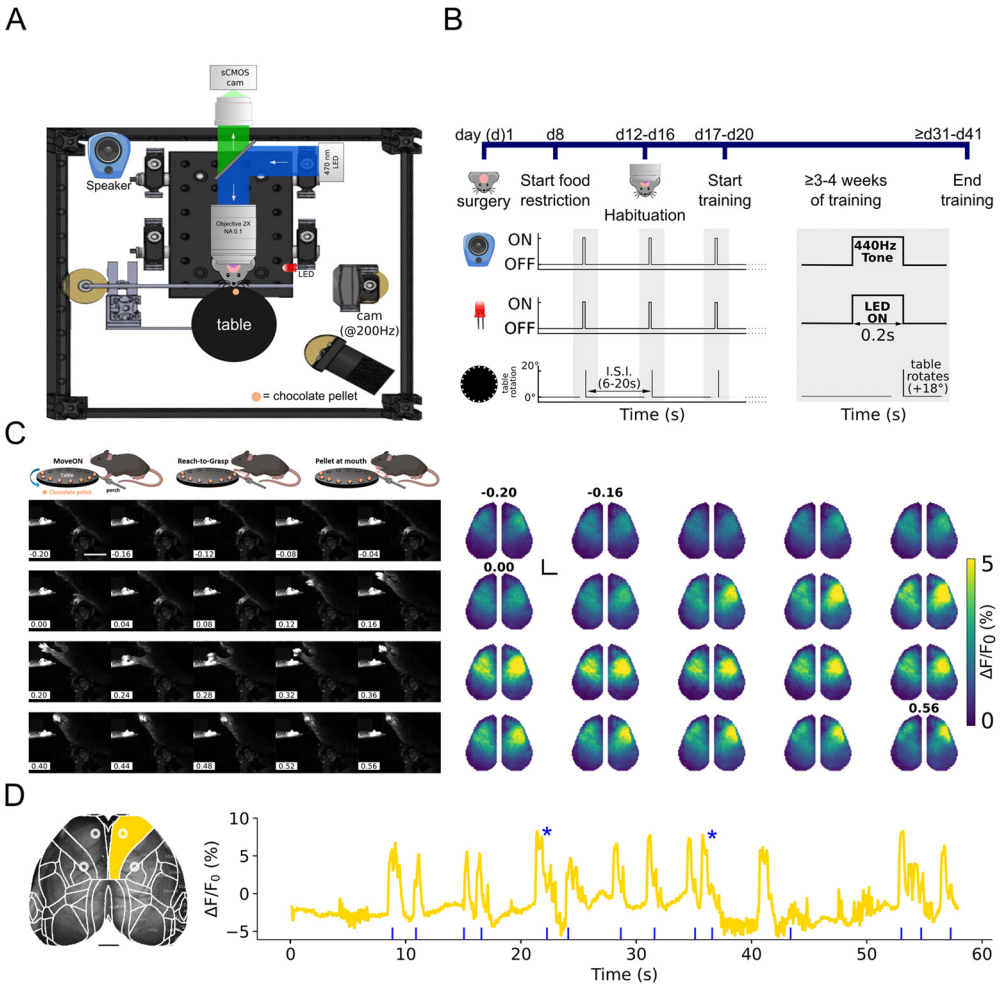

Figure 1. Mesoscale imaging of neocortical dynamics during RtGs. ***A***, Experimental setup. Schematics of the experimental setup, which comprises a custom-made widefield microscope to acquire images, 512 × 512 pixels, from the intact skull of *GCaMP6f* transgenic mice with a sampling rate of 25 Hz. Behavioral data were obtained via a high-speed (200 fps) camera placed on the left side of the head-fixed animal. Chocolate pellets were used to induce voluntary RtG movements. A turntable attached to a servo-motor was used for pellet delivery. All components of the experimental setup were synchronized by using a common TTL trigger. ***B***, Experimental timeline. Mice underwent surgery to expose the skull and head-bar implantation. Following recovery from surgery (~1 week), mice were food-restricted to 80%-90% of their baseline body weight and habituated to the experimental setup for at least 4 d (30 min a day/mouse). After habituation, mice were gently placed under the microscope and head-fixed below the objective. Training consisted of daily sessions (30-45 min/session) and lasted at least 3-4 weeks (5 sessions/wk). Each session consisted of several (at least 3) blocks, during which tones (square wave at 440 Hz) preceded by 200 ms the rotation of the turntable. Interstimulus interval (ISI) was between 6 and 20 s. ***C***, Mesoscale cortical activity during a single RtG movement. Top, Illustration of the movement sequence, that is, the onset of the RtG (MoveOn, left), the RtG (middle), and the finishing sequence of the RtG, when the pellet is brought to the mouth (pellet at mouth, right). Left, Image sequence of a mouse performing a successful RtG with the left forelimb. Right, Image sequence of cortical activity during the same perimovement epoch (between −0.2 and 0.56 s relative to the movement onset, sampling time 40 ms). Color bar (viridis) represents the range of ΔF/F0 (%). In this case, the movement lasts ~560 ms. Black dot represents bregma. Activity increases in both hemispheres during early phases of movement, while later increased activity is localized in the contralateral sensorimotor areas. Scale bar, 2 mm. ***D***, Neural activity in the right primary motor cortex is associated with repeated RtGs. Left, Image represents the typical FOV obtained during recordings. The Allen Mouse Brain Atlas mask was applied on the fluorescence image stacks to parcellate the signals according to the cortical areas of interest. For each hemisphere, areas of interest also included the RFA (top left ring and top right ring) and the CFA (bottom left ring and bottom right ring). Scale bar, 1 mm. Right, Graph represents the fluorescent and movement signals. ΔF/F0 (%) extracted from the right primary motor cortex (gold-colored trace). Blue rasterplot represents onsets of RtG movements. Increased activity in the selected cortical area is observed for each RtG attempt. Asterisks identify successful RtGs.

correlated with the ones used to characterize the neural activity (see below): mean speed (mm/s), max speed (mm/s), duration (s), pathlength (mm), number of speed peaks, mean acceleration (mm/s^2), and max acceleration (mm/s^2). The number of movement speed peaks was used as a measure of movement smoothness (Lai et al., 2015) and was defined as the number of peaks above the mean movement speed.

For the neural data, image stacks for each animal collected from different sessions were registered using custom-made software, by taking into account the bregma and λ position.

Raw wide-field imaging data of GCaMP fluorescence entail a non-negligible source of contamination because of hemoglobin, whose absorption spectrum largely overlaps with that of GCaMP, making interpretation of neural activity from these wide-field data challenging (Ma et al., 2016a). In order to account for the hemodynamic contribution, we first acquired widefield fluorescence data from the neocortex of *GFP* mice trained to execute RtGs. We expected the fluorescence signal from these mice to be static (i.e., not responsive to neuronal calcium levels); however, as reported elsewhere (Allen et al., 2017), fluorescence fluctuations were present in *GFP* mice around the movement onset (see Movie 3). We used the non-negative matrix factorization (NMF) as a source separation technique to demix the neuronal calcium signal from the non–calcium-related signal like hemodynamics. Among other source separation algorithms, we used the NMF because it has been previously used to calcium signals (Pnevmatikakis et al., 2016; Saxena et al., 2020) and because the weights and components are non-negative as opposed to other techniques, such as independent component analysis or singular value decomposition. For each animal, we concatenated the ΔF/F0 fluorescence sequences of any valid RtG considering a time window ranging

from −4 to 6 s around the movement onset (250 frames for each considered RtG). To avoid values of ΔF/F0 <0, which are required by the NMF, for those trials whose ΔF/F0 was <0, we found the minimum value for the entire stack in the time window and offset the trial by the same value so that the minimum value becomes zero. This image stack was then reshaped into a matrix F whose columns represent the number of frames in the stack (250 by the number of considered RtGs) and its rows represent the number of pixels of the each frame (40,000 = 200 × 200). We then used the NMF to factorize the fluorescent stack of each animal into two matrices W and H by setting the numbers of components to 40.

Where W is the component matrix whose columns equal the number of components and the same number of rows of F which represent the pixels of each frame, H, instead, represents the weight matrix and represents the coefficient to assign to each component to reconstruct the original fluorescence stack. We then analyzed each component of the W matrix by reshaping it into a 200 × 200 pixels image. We considered components to be non–calcium-related like hemodynamics if: (1) the component highest activation matches the superficial vasculature observed from the raw fluorescence image; (2) the components highest activation lays on the edge of the mask where the skull starts to form the temporal bones; and (3) the component was considered to be noisy (i.e., activation was low and spread over large portion of the cortical mantle). We then demixed the neuronal calcium signal from the non–calcium-related signal by setting to 0 the columns of W that met one of the three abovementioned conditions.

To remove the offset introduced by summing the minimum before applying the NMF, we subtracted the ΔF/F0 in the time window −2 to −0.5 s. The signal was then low-pass filtered (9 Hz) to reduce the unwanted contribution of respiratory and heartbeat components. The comparison between the raw and the resulting denoised signal for the GCaMP and *GFP* mice is in Movies 2 and 3, respectively.

To dissect the contribution of each cortical area for RtG, the processed stacks we also registered the cortex to the surface of the Allen Institute Mouse Brain Atlas (www.brain-map.org) projected to our plane of imaging. We further applied a mask to exclude the medial-most areas because they lay over the superior sagittal sinus; therefore, the neuronal signal in this region could be more easily affected by hemodynamic artifacts. Areas laying on the most lateral parts of the mouse cortex were also excluded. This parcellation of the neocortex created 22 areas for each hemisphere, for a total of 44 areas, plus the left neocortical hemisphere, the right neocortical hemisphere, and both hemispheres (CTX). The abbreviations and extended names for each areas are as follows: MOs, secondary motor area; RFA, rostral forelimb area; MOp, primary motor area; CFA, caudal forelimb area; SSp-bfd, primary somatosensory area, barrel field; SSp-ll, primary somatosensory area, lower limb; SSp-m, primary somatosensory area, mouth; SSp-n, primary somatosensory area, nose; SSp-tr, primary somatosensory area, trunk; SSp-ul, primary somatosensory area, upper limb; SSp-un, primary somatosensory area, unassigned; SSs, secondary somatosensory area; RSPagl, retrosplenial area, lateral agranular part; RSPd, retrosplenial area, dorsal part; VISrl, rostrolateral visual area; VISa, anterior visual area; VISal, anterolateral visual area; VISam, anteromedial visual area; VISl, lateral visual area; VISli, laterointermediate visual area; VISp, primary visual area; and VISpm, posteromedial visual area. The coordinates for CFA (AP: 0.2 mm; ML: 1.7 mm) and RFA (AP: 2.3 mm, ML: 0.9 mm) were determined herein as the average of the coordinates reported in recent papers (Tennant et al., 2011; Hira et al., 2013; Morandell and Huber, 2017; Wang et al., 2017). Throughout the text and figures, we added the suffix L and R to term cortical areas of the left (ipsilateral with respect to the paw executing the movement) or right (contralateral with respect to the paw executing the movement), respectively (e.g., MOs_L, MOs_R). For each block, the image stacks were processed to obtain the estimates of $\Delta F/F_0$. Briefly, the image stacks were processed considering the equation $\Delta F/F_0 = (F - F_0)/F_0$, where F defines the value of the fluorescence signal in a given moment and F_0 defines mean fluorescence over each block. Neocortical areas were considered associated with movement if their activity during any moment of the time window crossed a threshold defined as the mean + 1.96 × SD of the neural signal occurring during the baseline (−2 to −1 s with respect to MoveON). The highest value reached at any moment in the time window −2 to 1.5 s around MoveON was defined as the PeakMax. Also, to statistically determine whether the transaction between the behavioral phases is associated with different neural activity levels, we used a two-way mixed-model ANOVA followed, if appropriate, by Tukey's HSD *post hoc* tests. To

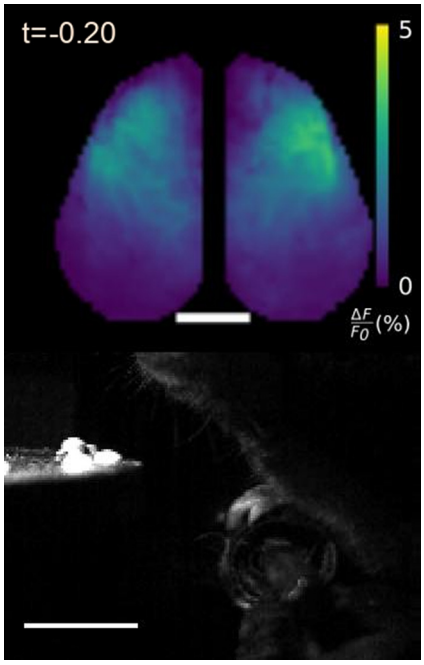

Movie 1. Example of a typical RtG movement (bottom) performed by a GCaMP6f mouse and the related neocortex-wide activity (top). In the movie, the fluorescence activity increases before and throughout the RtG, with a mediolateral spread across sensorimotor regions of both hemispheres. Top, Color bar (viridis) represents the range of $\Delta F/F_0$ (%). Scale bar, 2 mm. Bottom, Scale bar, 10 mm. Time (t, in seconds) for both sequences is shown at the top. [View online]

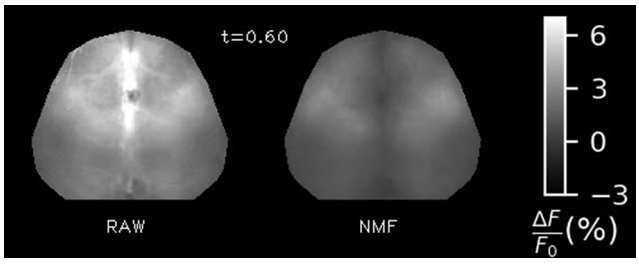

Movie 2. Image sequences of fluorescence activity across the neocortex before (RAW, left) and after NMF correction (NMF, right) for GCaMP mice. Time (t, in seconds) for both sequences is shown at the middle. [View online]

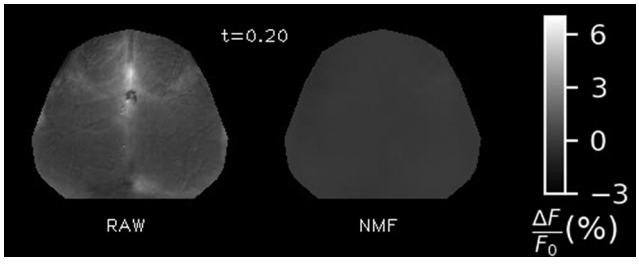

Movie 3. Image sequences of fluorescence activity across the neocortex before (RAW, left) and after NMF correction (NMF, right) for *GFP* mice. Time (t, in seconds) for both sequences is shown at the middle. [View online]

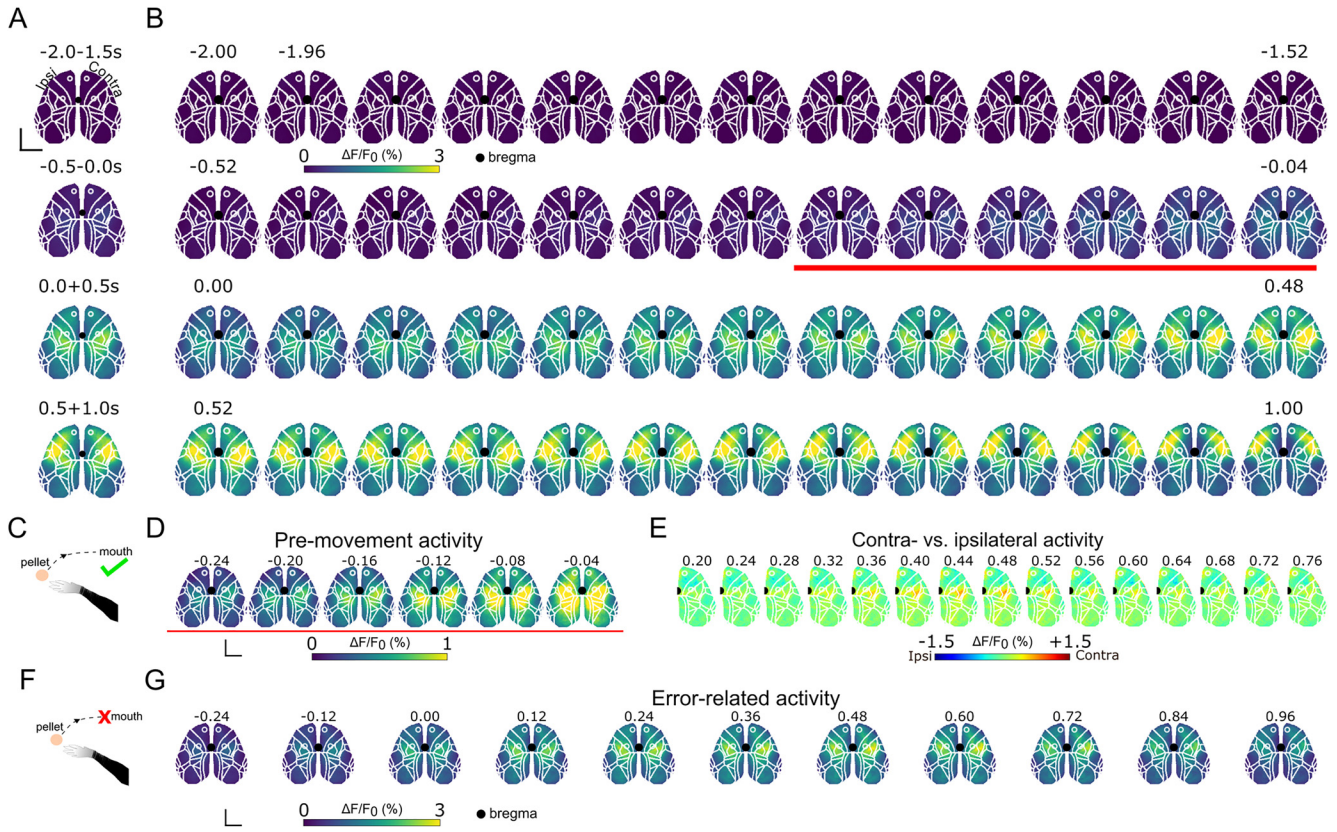

Figure 2. Single-pixel analysis of neocortex-wide activity during successful and error RtGs. ***A***, Top, Averaged activity across the temporal windows −2, −1.5 s; −0.5, −0.04 s; 0, 0.5 s; and 0.5-1 s relative to MoveON. Black dot represents bregma. Scale bar, 2 mm. ***B***, Perievent (−2 + 2 s with respect to MoveON) image sequence for successful RtGs. Images represent the average signal obtained from aligned stacks of all subjects, for all perimovement epochs ($n = 78$ movements, 6 mice). On average, activity increases before movement onset in medial regions of the cortex and spreads mediolaterally thereafter (images above the red line, and in ***D***). This increase involves areas of both hemispheres. Color bar (viridis) represents the range of $\Delta F/F_0$ (%). ***C***, Diagram represents a successful RtG (i.e., an RtG that does end with the pellet eaten). ***D***, Premovement activity starts in medial areas and spreads laterally during RtGs. Scale bar, 2 mm. ***E***, Contralateral versus ipsilateral activity across the neocortex during successful RtGs. Neocortex-wide activity is compared between the ipsilateral and contralateral hemispheres. Perievent (0.20 + 0.76 s with respect to MoveON) image sequence for successful RtGs. Images represent the average signal obtained from aligned stacks of all subjects, for all perimovement epochs ($n = 78$ movements, 6 mice). On average, activity appears distributed across both hemispheres. A pronounced bias toward the contralateral hemisphere emerges around the RFA and around the SSp-ul and part of the CFA and SSp-ll, from 0.36 to 0.56 s after MoveON. Color bar (jet) represents the range of $\Delta F/F_0$ (%). ***F***, Diagram represents an error RtG (i.e., an RtG that does not end with the pellet eaten). ***G***, Perievent (−0.24 + 0.96 s with respect to MoveON) image sequence for error RtGs. Images represent the average signal obtained from aligned stacks of all subjects, for all perimovement epochs ($n = 113$ movements, 6 mice). In error RtGs, compared with successful RtGs, during the latter phase of movement execution, the activity does not involve lateral areas across both hemispheres. Color bar (viridis) represents the range of $\Delta F/F_0$ (%). Scale bar, 2 mm. Time is in seconds (s) for all image sequences.

determine the temporal involvement of neocortical areas during the task, we computed the latency necessary to reach the 50% and the 100% of the PeakMax (latency to *HalfPeakMax* and latency to *PeakMax*, respectively) in each of the responsive areas. Finally, to quantify the rate of rise of the neural response in each area, we quantified the slope of the neural response as $\frac{PeakMax90 - HalfPeakMax}{LPeakMax90 - LHalfPeakMax}$ where PeakMax90 is the 90% of the PeakMax and LPeakMax90 and LHalfPeakMax are the times where the signal reaches 90% and 50% of the PeakMax, respectively.

To evaluate the FC between the areas during RtGs, cross-correlations between pairs of areas for each behavioral phase were computed at the single-trial level. The fluorescent time series were chunked according to the behavioral phase of interest and are presented as cross-correlation matrices (CCMs). We investigated the network membership of these regions by using a hierarchical clustering algorithm (HCA) that was based on Ward's linkage method (Ward, 1963), which minimizes the variance between the clusters. The proximity was then interpreted as an indirect measure of FC and represented graphically by means of dendrograms. All data are reported as mean ± SD if not stated otherwise. Sample size and appropriate statistical analyses are specified in each figure legend. Statistical significance was defined as $\alpha < 0.05$ if not stated otherwise. Multiple comparisons were corrected by Bonferroni or Bonferroni–Hochberg procedures. No statistical methods were used to predetermine the sample size. All statistical analyses and related figures were created using either Python or R and were assembled in Inkscape.

Results

Wide-field calcium imaging during RtG

We conceived that, for a mouse to perform complex, goal-directed movements, such as RtG, a specific neural network within the neocortex could be recruited. To gain information about such dynamics, our setup integrates a large FOV microscope to simultaneously image the entirety of the neocortical surface and a behavioral apparatus for inducing, delivering, and videotaping the RtGs (Fig. 1*A*). Mice were trained to perform the task while head-fixed under the microscope (Fig. 1*B*). Once trained, animals executed RtG movements to eat chocolate pellets that were placed on a rotating table placed in front of them (Fig. 1*C*, left). The time-aligned image stacks obtained from the camera and from the microscope allowed the monitoring of neural activity across functional areas of the neocortex, throughout the behavioral task, with activity increasing in contralateral regions, and to a lesser extent for the ipsilateral sensorimotor regions (Fig. 1*C*,*D*; Movie 1).

Neural activity increases across several areas spanning both hemispheres during successful RtG behavior

Single-pixel analysis of cortex-wide activity indicates that, on average, for all successful RtG movements (Fig. 2) executed by all subjects, the neural activity increases bilaterally in the neocortical mantle. The contralateral hemisphere displayed higher activity compared with the ipsilateral one only in a small portion of the cortex; at the rostral portion of the secondary motor cortex, and in the sensorimotor cortex with peak activity centered around the upper limb somatosensory cortex (Fig. 2*E*). We averaged the different contributions of neocortical activation during four temporal windows (i.e., at 2-1.5 s and at 0.5-0.04 s before MoveON, at 0-0.5 s, and at 0.5 + 1.0 s after MoveON; Fig. 2*A*,*B*) showing that activity increases in the −0.52 to 0.04 s window and lasts up to 1 s. In particular, premovement activity irradiated from medial to lateral regions of both hemispheres to (Fig. 2*D*) and during movement, bilateral activation in more rostromedial areas becomes apparent with more pronounced activity in the contralateral hemisphere ~0.24-0.48 s after movement onset (Fig. 2*A*). Instead, later (>0.48 s) phases of movement activity are characterized by an increase in neural activity in the rostro-lateral regions of both hemispheres. When considering all windows together, it is clear that neural activity for successful RtGs spreads over a wide portion of the cortical mantle.

When considering unsuccessful RtGs, we observed a different activation pattern with respect to successful ones (Fig. 2*F*,*G*). In particular, neural activity during errors diverged from correct trials starting at 0.38 s and is characterized by low values of ΔF/F0. In addition, even if activity originated bilaterally in medial regions as in successful RtGs, the neural response was shorter and did not spread to the rostro-lateral regions as in successful RtGs.

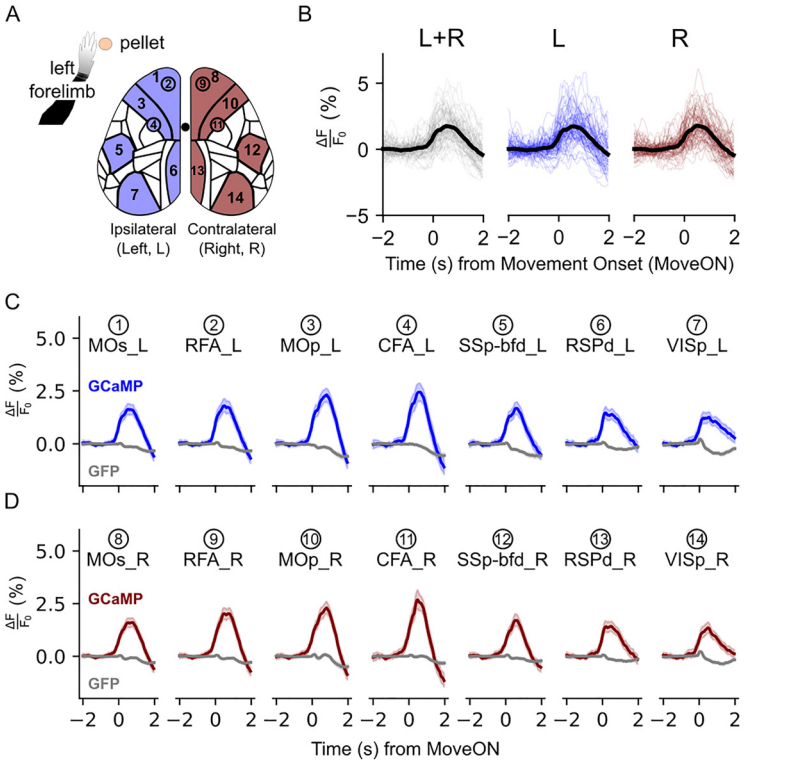

Figure 3. Global increase of neural activity during RtGs. ***A***, Illustration of the areas from which the traces displayed in ***B*** were obtained, which include also the RFA and the CFA. Areas and subsequent traces are color-coded accordingly to the left (blue) and right (red) hemisphere, whereas the numbers are associated with the areas in ***C*** and ***D***. Neural activity traces refer to the perimovement epochs ($n = 78$ movements, 6 mice). ***B***, $\Delta F/F_0$ (%) traces of single trials (thin colored lines) and their corresponding average (thick black line) for the whole cortex (L + R), the ipsilateral (left, L) and the contralateral (right, R) hemisphere, for a time window of −2, 2 s around the movement onset (MoveON). ***C***, ***D***, Traces of neural activity for a selection of 14 areas across the two neocortical hemispheres for GCaMP mice (blue traces and red traces) and for *GFP* mice (gray traces). The MOs, RFA, MOp, CFA, and RSPd, and to a lesser extent the SSp-bfd and the VISp, display increased activity levels during RtGs. Shaded regions represent 95% CIs for the population mean. The comparison between the raw and the denoised signals for the GCaMP and *GFP* mice is shown in Movies 2 and 3, respectively.

To characterize the contribution of functional areas across the neocortex during successful RtG, we parcellated the acquired image stacks according to the Allen Institute Mouse Brain Atlas (Fig. 3*A*, left). The resulting parcellation allowed to extract the calcium signal for each neocortical area. The increase in the levels of neural activity encompassing the neocortical mantle is observed also on each hemisphere separately (Fig. 3*B*). Several areas displayed a vigorous increase in neural activity levels with movement execution, including the motor areas and the retrosplenial cortices of both hemispheres, whereas other areas, such as the SSp-bfd, displayed a more modest increase in activity (Fig. 3*C*,*D*). Overall, the activity levels across homologous areas of both hemispheres, including motor, somatosensory, retrosplenial, and visual areas, appeared comparable.

Calcium signals from neocortical areas increase before movement onset

We compared the temporal profile of the parcellated fluorescent calcium signal across the peri-event time window. Of the areas considered, all ($n = 44$) emerged as associated with movement (i.e., showed activity levels higher than the set threshold) with the primary and secondary motor areas displaying the highest PeakMax and other areas spread across both hemispheres, forming a distributed cortical network associated with RtG movements (Fig. 4*A*). Across all responsive areas, the HalfPeakMax was reached before movement onset, which indicates that the increases in the amplitude levels of the fluorescent signal anticipate the movement onset (Fig. 4*B*, left). In addition, across all responsive areas, we found that the first time point passing the threshold occurred well before movement onset (580 ± 113 ms). These results suggest that the temporal dynamics of the calcium signal detects variations in the levels of neural activity also in the RtG premovement phase. Moreover, the latency to reach the HalfPeakMax showed low variability across areas. In contrast, the latency to reach PeakMax occurred after the movement onset for all areas and differed across areas (Fig. 4*B*, right). In particular, somatosensory areas and the contralateral CFA reached the PeakMax later, compared with other areas. Next, we compared the neural activity levels across the three temporal windows (rest: −2 to 1.5 s; premove: −0.5 to 0.04 s; move: 0 to 0.5 s), across neocortical areas (Fig. 4*C*). We found that both the time window and the areas significantly affect the calcium responses [two-

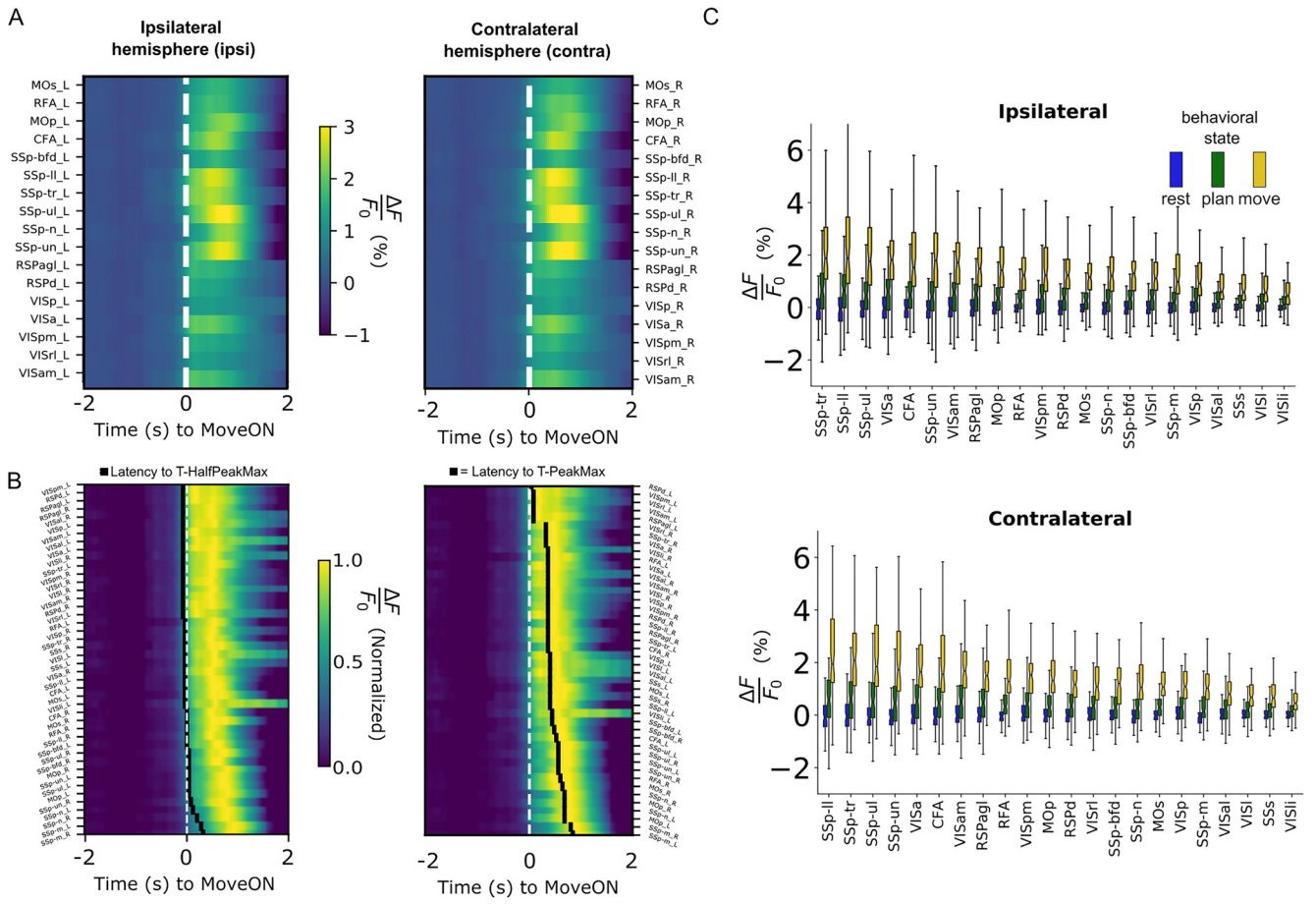

Figure 4. Bilateral and state-associated neural dynamics emerge during RtG. ***A***, Color plots represent the mean activity for all neocortical areas, separated for each hemisphere (ipsi = left, ipsilateral hemisphere, on the left; contra = right, contralateral hemisphere, on the right side). Several homologous areas across the hemispheres exhibit increased activity levels. Color bar represents the levels of $\Delta F/F_0$ (%) activity. ***B***, Color raster plots represent the mean, normalized activity for the movement-associated areas. Left, The areas in the plot are ranked by latency to reach T-half max%, in ascending order (areas requiring less time to reach the T-half max% are placed higher in the plot). Black squares represent the latency to T-half max% for each area. Right, The areas in the plot are ranked by latency to reach the PeakMax, in ascending order (areas requiring less time to reach their PeakMax are placed higher in the plot). Black squares represent the latency to T-half max% for each area. ***C***, Emergence of a state-associated increase of activity levels across neocortical areas. Notched boxplots (top and bottom whiskers represent maximal and minimal value, respectively, excluding outliers) represent the activity levels for all movement-responsive areas, ranked based on PeakMax, ranked by descending median value, from left to right. Left, Movement-responsive areas within the ipsilateral hemisphere. Bottom, Movement-responsive areas within contralateral hemisphere (Extended Data Fig. 4-1).

way mixed model ANOVA, effect of temporal window, $F_{(1.89,6392.37)} = 2824.784$, $p < 0.0001$, temporal window × area interaction, $F_{(81.13,6392.37)} = 7.786$, $p \leq 0.0001$, Bonferroni *post hoc* tests]. *Post hoc* pairwise comparisons indicate statistically significant increases from rest to movement for several areas, including the MOs, the RFA, the MOp, the CFA, the RSPd, the SSp-ul, and the visual areas. These increases were found to be already present when comparing the rest versus the premove window (e.g., for the MOs, the RFA, the MOp, the CFA, the RSPd, and the SSp-ul) but were found not to be different for few areas, including the SSp-bfd and the several visual areas (for all pairwise comparisons, see the Extended Data Fig. 4-1). These findings suggest that a global network of areas is activated during movement execution, with the majority of them increasing their levels of activity before movement onset.

Movement onset transiently increases FC

Considering the increase in neural activity levels across the areas from rest to movement, we next asked whether such variation was associated with a modulation of FC across areas and whether FC was modulated throughout the behavioral phases. The hierarchical cluster analysis (HCA) revealed that near movement onset there is an increase in FC. Indeed, we found that the Ward distance was lowest around MoveON (−0.28 s, time window length = 0.48 s; Fig. 5, middle, left inset), indicating that the areas tend to form a single functional aggregate. This effect is illustrated by the CCM (Fig. 5, middle, right), indicating an overall increase in the correlation coefficients around MoveON. Conversely, during movement execution ("Grasp"), the FC decreases (Fig. 5, bottom, right), leading to the emergence of four distinct clusters (Fig. 5, bottom, left). The first cluster contained the caudal portion visual areas only and therefore could be regarded as a visual network. The second cluster included intermingled areas: that is, two subdivisions of the visual cortex (VISam and VISa), the retrosplenial cortices (RSPd and RSPagl), several somatosensory areas, as well as the CFA thus could be considered as a multimodal network. The third cluster was formed by two areas of the primary somatosensory cortex related to the mouth and nose representation (i.e., the SSp_m and the SSp_n). Finally, the last cluster is constituted by two somatosensory areas, including the one associated with the representation of the upper limbs (SS-p_ul) as well as an adjacent area with an unknown association (SS-p_un) as well as the primary and secondary motor areas and the RFA and could be regarded as the sensorimotor network.

Because the used parcellation may not account for subfield-specific FC, we next sought to determine whether such a scheme of communication is maintained in the context of single-pixel analysis. To this end, we used seeds of the contralateral hemisphere that affiliated with the four clusters emerging during the grasping phase to compute the single pixel seed correlations shown in Figure 5. Overall, the seed correlations are in good agreement with the results of the HCA, and both show that the transition from resting to movement execution was associated with a robust increase in the cross-correlations around movement onset (Fig. 5, right).

Our approach provides evidence for the existence of segregated functional networks emerging during motor execution. Overall, these FC results suggest that the corticocortical communication scheme during goal-directed forelimb movements can be decomposed into two parts: the earlier phase, with a transient increase in cross-correlation; and a latter phase, where separated networks emerge.

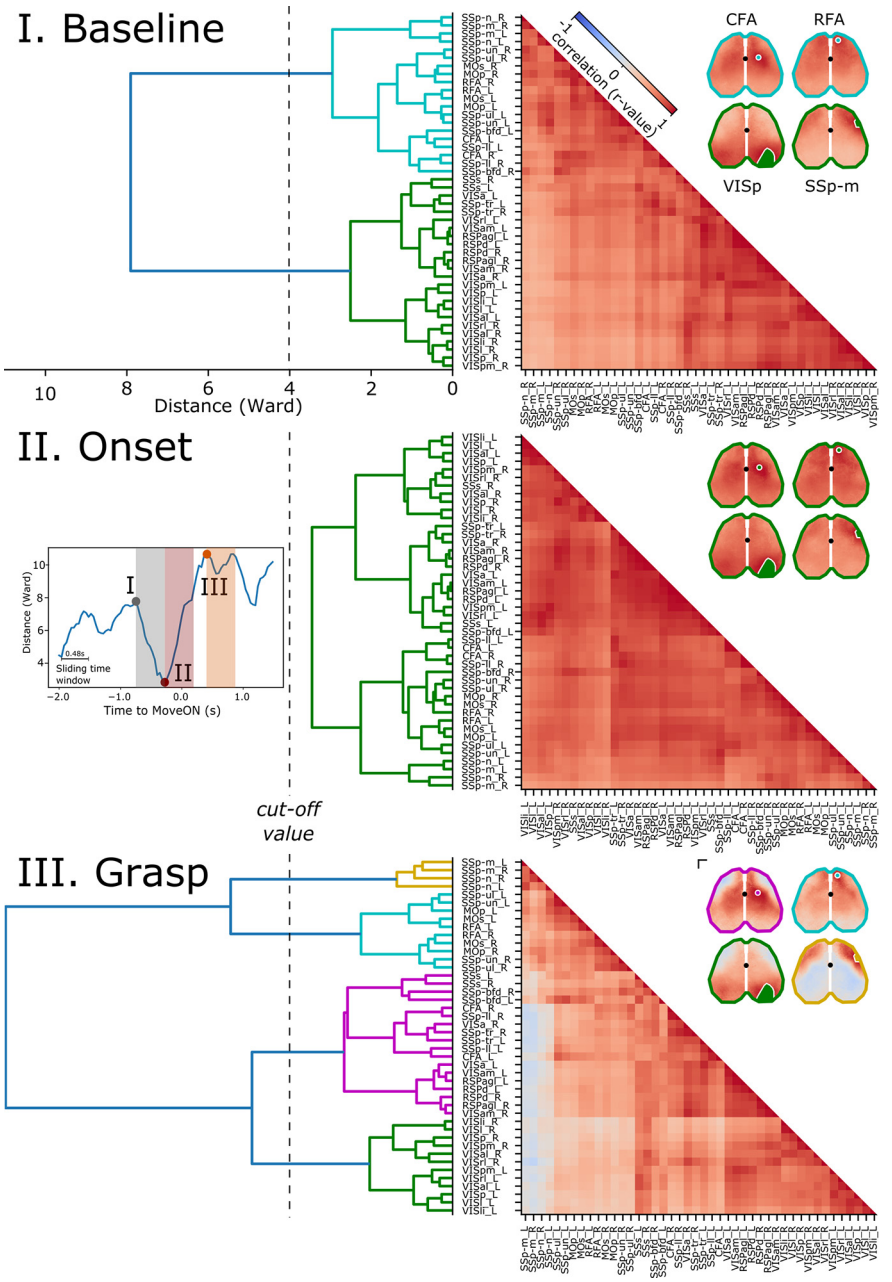

Figure 5. Movement onset is associated with transient increases in FC. FC was analyzed by means of HCA and CCM, for three temporal windows (top, I, Baseline: −0.76 to 0.26; middle, II, Onset: −0.32 + 0.28; bottom, III, Grasp: 0.4-0.9 s with respect to MoveON), which were defined using a sliding time window yielding the highest and lowest Ward values, left inset. A strong decrease in the Ward values is observed from the baseline (I) to the onset (II) phase. This decrease is transient, as during the grasp phase (III) there is an abrupt shift toward rearrangement of the FC, shown by high Ward values. An equal cutoff was chosen for each temporal window, and the resulting clusters are color-coded in the figure based on the four clusters emerging during the grasp phase. The first cluster (green) contains visual areas. The second (magenta) is comprised of a heterogeneous set of areas, including the somatosensory areas, both RFA and CFA, some visual areas, and all the RSPs. The yellow cluster includes the somatosensory areas of the mouse's snout, whereas the last cluster (cyan) consists of the MOs, MOp, SSp-ul, and SSp-un. During the grasp phase, some areas maintain highly positive cross-correlation values. A trend toward anticorrelation arises between the areas representing the mouse's snout. For each CCM, insets represent the seed-pixel analysis (SCA) for four areas: seeds, which represent the four clusters emerging during the III phase. This analysis also highlights that during the grasp phase two anticorrelated networks emerge across both hemispheres. Correlation coefficients (CC; −1 indicates anticorrelation, 1 indicates correlation) are color-coded (cool warm color map). Black dots represent bregma. Scale bar, 1 mm for all insets.

Movement kinematics correlates with neural activity levels in sensorimotor areas of both hemispheres

Considering the increase in activity observed across the neocortical areas, we sought to determine the extent of association between neural activity and movement parameters. To this end, we first reconstructed the spatial trajectories for the successful RtGs and computed the movement metrics (Fig. 6*A–C*). The movement distance was 54.54 ± 18.81 mm (Fig. 6*D*), the movements lasted 0.71 ± 0.26 s (Fig. 6*E*), while the number of speed peaks was 17.78 ± 7.99 (Fig. 6*F*).

Since during movement execution we observed the emergence of differentiated activation among areas, we asked to what extent each area contributed to specific kinematic parameters of RtG movement. To this end, we performed correlation analyses between neural activity measures in all responsive areas of the neocortex and the extracted parameters of movement kinematics (Fig. 7). Differently from the activity levels, which were broadly increased across the neocortical mantle, statistically significant correlations between neural activity and movement kinematics were found only for few areas across both hemispheres (Fig. 7*A*). Specifically, our analysis revealed a negative correlation between the amplitude of the signal (PeakMax) and movement smoothness in the MOp, the CFA, the SSp-ul, and the SSp-un of the ipsilateral hemisphere (number of speed peaks, $\rho = -0.40$, $p_{adj} < 0.01$; $\rho = -0.49$, $p_{adj} < 0.01$; $\rho = -0.41$, $p_{adj} < 0.01$; $\rho = -0.39$, $p_{adj} = 0.02$ for MOp, the CFA, the SSp-ul, and the SSp-un,

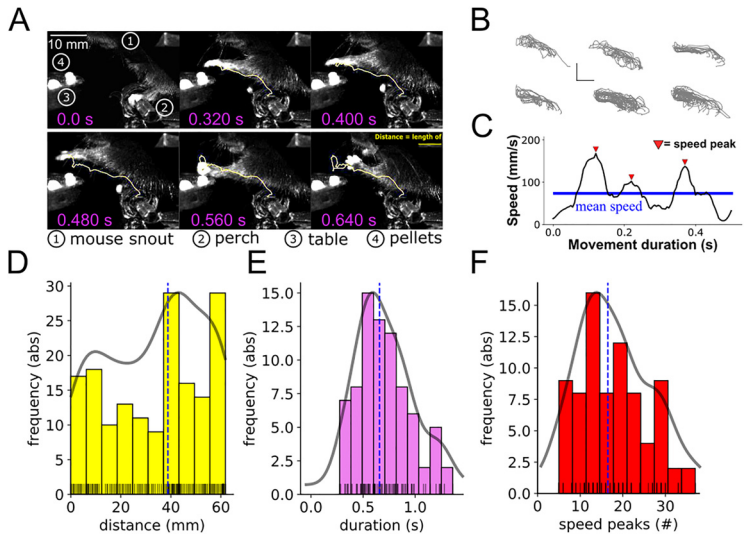

Figure 6. Kinematic trajectories of successful RTGs. ***A***, Example of RtG movement tracked for reconstruction and kinematic analysis. In this stereotypical RtG sequence, the yellow line in each image indicates the path covered by the metacarpus. Selected components of the setup are labeled with numbers for display purposes (for more details on the setup and the behavioral task, see Fig. 1). ***B***, Reconstructed RtG trajectories of left-paw movements for each animal. Trajectories of successful movements are shown, separated for each animal. Scale bar: both directions, 10 mm. ***C***, Speed profile reconstruction from a successful RtG movement. Speed peaks exceeding the mean speed (horizontal blue line) are used to compute the movement smoothness (red triangles). ***D***, Distribution of the movement distance. Histogram (bin size = 10) represents the absolute frequency distribution for the distances (arc length) covered by the paw to reach the chocolate pellet and eat it. Vertical line indicates the median value. Shaded curve indicates the density distribution. Lines of the rug plots (bottom) indicate the raw distribution for each movement. ***E***, Distribution of the movement duration. Histogram (bin size = 10) represents the absolute frequency distribution for the movement durations. Vertical line indicates the median value. Shaded curve indicates the density distribution. Lines of the rug plots (bottom) indicate the raw distribution for each movement. ***F***, Distribution of the number of speed peaks. Histogram (bin size = 10) represents the absolute frequency distribution for the speed peaks. Vertical line indicates the median value. Shaded curve indicates the density distribution. Lines of the rug plots (bottom) indicate the raw distribution for each movement (the speed peaks being computed as natural numbers, overlap frequently in the rug plot).

respectively; Fig. 7*B*). Also, in the ipsilateral CFA, the PeakMax was inversely correlated with the movement pathlength (Fig. 7*D*). In the contralateral RFA, we found that the slope of the neural response was inversely correlated with movement pathlength ($\rho = -0.54$, $p_{adj} < 0.01$; Fig. 7*C*). In this area, the latency to reach the PeakMax correlated with movement smoothness ($\rho = 0.46$, $p_{adj} < 0.01$) and pathlength ($\rho = 0.43$, $p_{adj} < 0.01$; Fig. 7*D*), while the slope was inversely correlated with movement smoothness ($\rho = -0.51$, $p_{adj} < 0.01$; Fig. 7*D*). Similarly, the latency to reach the PeakMax in the contralateral MOp and in the CFA was anticorrelated with respect to movement speed ($\rho = -0.47$, $p_{adj} < 0.01$ and $\rho = -0.43$, $p_{adj} < 0.01$, for MOp and for the CFA, respectively; Fig. 7*C*). At variance with all the other areas, the degree of movement smoothness was positively correlated with the latency to reach the PeakMax in the contralateral SSp-ll ($\rho = 0.41$, $p_{adj} < 0.01$). Therefore, while neural activity level increases neocortex-wide, a restricted group of rostral areas exhibit activity that correlates with kinematic parameters of RtGs.

Discussion

We provided an unprecedented view of the mesoscale level neocortical dynamics from mice performing an RtG task. To the best of our knowledge, this is the first reported step toward an optical characterization of neocortex-wide neural dynamics in rodents during voluntary RtG movement planning and execution. Our work provides novel evidence for the role played by the secondary motor areas during RtG and, by directly observing all areas of the neocortex, an integrative framework not reported previously.

Our results point the attention also to areas beyond the MOs, the MOp, and their subdivisions (RFA and CFA) toward other territories, such as the RSC, the SSp, and the visual areas, which were previously not recorded and studied simultaneously within the context of the RtG. For the RSC, while its participation to RtG in the mouse is demonstrated here for the first time, the contribution of RSC may be explained by its known involvement in the processing of visual information necessary to locate the target relevant for the behavioral tasks (Czajkowski et al., 2014). Indeed, RSC is involved in early phases of learning (Makino et al., 2017); however, no information was available about the corticocortical interactions (e.g., with the secondary motor areas) and about the relationship with kinematic parameters of movement.

The global activation found in the present work is consistent with recent reports on other types of behavioral tasks (Goard et al., 2016; Wekselblatt et al., 2016; Allen et al., 2017; Kyriakatos et al., 2017; Makino et al., 2017; Musall et al., 2019; Stringer et al., 2019; Salkoff et al., 2020); here we extended it to the RtG. In addition, we show that this activation is supported at the trial-by-trial level by an increase in FC occurring at movement onset. Indeed, our HCA revealed that such an increase in FC represents the transition between the premovement and postmovement onset FC clusters whose correlation maps have been observed previously in the mouse (Vanni et al., 2017; Hakon et al., 2018; Clancy et al., 2019) and closely related to the underlying structural connectivity (Hakon et al., 2018). Therefore, such widespread activation would raise the possibility that neocortical activation patterns for the production of successful RtG movements are distributed rather than localized.

In interpreting our results, we cannot exclude that whole-body movements may account for part of the widespread distribution of neocortical activity we observe during RtG. However, it is important to note that, because of the trial averaging around the movement onset, such movements have to be performed by each animal in a substantial number of trials to contribute to the spread of the response. Also, other parameters, such as arousal, could possibly contribute to the increased activity we observed in visual areas. Indeed, it was shown that the levels of activity in the visual cortex are related to arousal (Stringer et al., 2019).

Recent work emphasizes that it is critical to understand both functional specialization and functional integration schemes and how they relate to different aspects of complex behavior (Cohen and D'Esposito, 2016). Our work thus shows the first direct evidence indicating that, while neural activity increases globally during RtG, neuro-kinematic correlations are significant only for a subset of rostral areas. The present findings are in agreement with Salkoff et al. (2020), in which it was shown that these areas encode performance in a "simple" licking behavior. The present results suggest that forelimb movement planning and execution

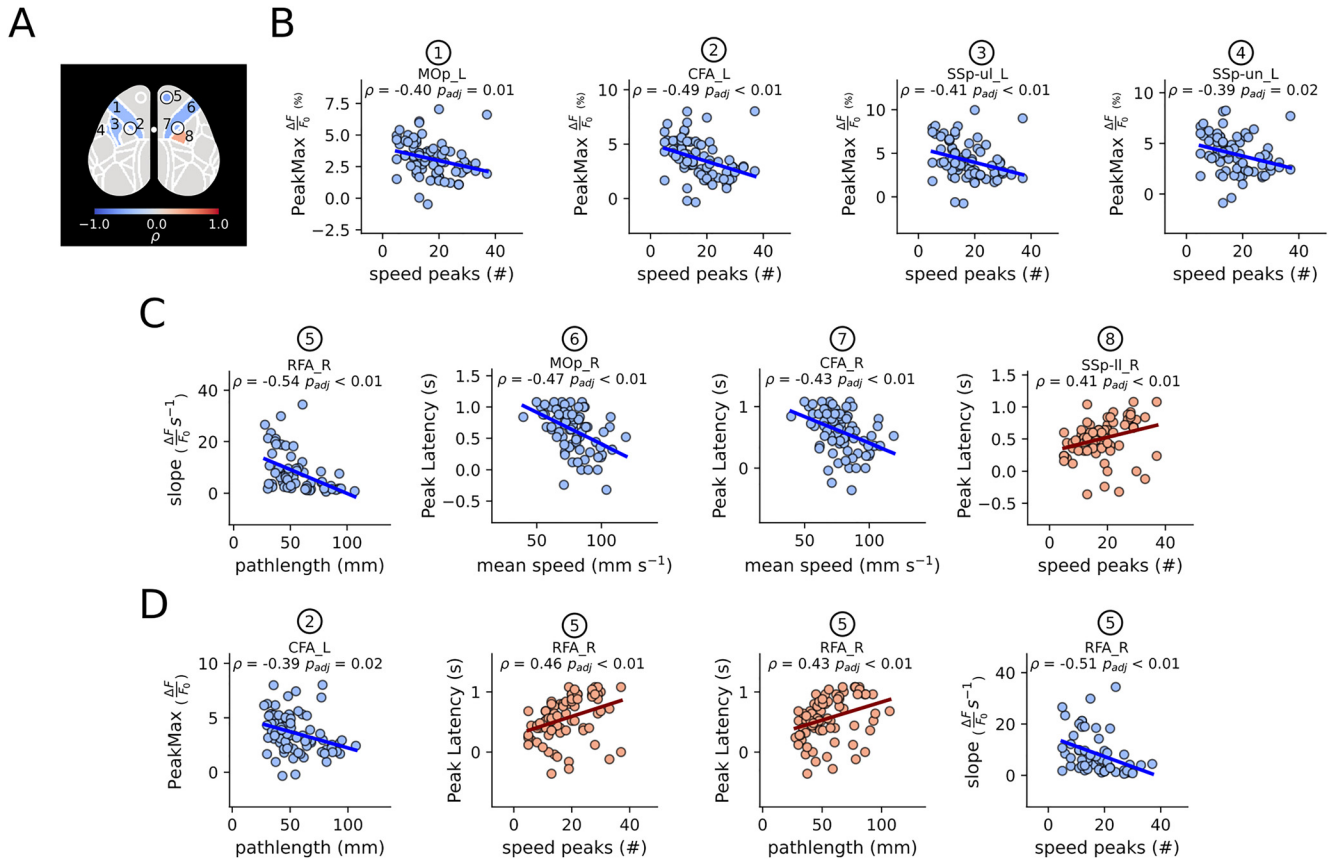

Figure 7. Local neural activity levels in sensorimotor areas correlate with movement kinematics. ***A–C***, At variance with the widespread activity associated to RtG movements, only 8 areas were found to have a statistically significant correlation with movement kinematics. Color bar represents the correlation coefficient. The neural activity in the majority of these areas, that is, the RFA, the MOp, the CFA for the ipsilateral (left) hemisphere and the RFA and MOp for the contralateral neocortex, was anticorrelated with respect to movement kinematics. At the contrary, the activity in the right SSp-ll positively correlated with speed peaks. ***D***, Additional neuro-kinematic correlations in the ipsilateral CFA and in the contralateral RFA. The PeakMax in the ipsilateral CFA is negatively correlated with movement distance ("pathlength"). The latency to reach the PeakMax in the contralateral RFA correlated with both the movement smoothness ("speed peaks") and the movement distance ("pathlength"). The slope in the contralateral RFA negatively correlated with the movement smoothness. For the correlation analysis of each pair of parameters, we set a Benjamin–Hochberg significance level of $\alpha < 0.05$.

may involve large neural networks across the neocortex while the encoding of kinematic parameters occurs primarily in segregated areas. However, being correlational in nature, our work will be likely instrumental for guiding optogenetic interventions, to gain insight about the causal role of each neocortical area during voluntary movements. Nonetheless, such direct observation of global and local activation patterns for dexterous movements provides an integrated view of the nature of information processing in the mouse neocortex and encourages future investigations toward decoding of behavioral parameters from neural data, a computational approach that is increasingly used on fluorescent imaging data of neural activity (Prsa et al., 2017; C. Li et al., 2019; Salkoff et al., 2020).

Our data add experimental evidence to the relatively new idea of ipsilateral representation of movement parameters, supporting recent work in rodents, where recordings restricted to the posterior parietal cortex recently reported evidence for ipsilateral control of limb movement (Soma et al., 2019). Indeed, ipsilateral activity is also a computational feature of the human neocortex and is increasingly getting attention in the motor control community (Bundy et al., 2018; Bundy and Leuthardt, 2019).

While the correlation between movement kinematics and ipsilateral activity during RtG came as a surprise, there is a growing literature suggesting that neocortical dynamics concerning the generation of contralateral and ipsilateral limb movements are controlled by both hemispheres (Mutha et al., 2013; Schaffer and Sainburg, 2017; Heming et al., 2019). In this regard, our results on both contralateral and ipsilateral activation and correlations with movement kinematics for RtG control support this bihemispheric model of forelimb control.

Our findings extend these studies by providing evidence for a correlation between large scale, area-level activity, and specific metrics of RtG movements. Our findings also encourage to study, at the cellular level, the role of areas found to be active during movement (e.g., the visual areas) less intensively studied in the association to forelimb movements (Morandell and Huber, 2017; Ebina et al., 2018; Galinanes et al., 2018). In the future, it would also be relevant to assess the neocortical dynamics during RtG in a freely moving condition or during performance refinement (Makino et al., 2017; Whishaw et al., 2017; Bollu et al., 2019; Hwang et al., 2019).

Moreover, movement errors are associated with altered activity in the motor and parietal cortex (Diedrichsen et al., 2005); however, information on neocortex-wide dynamics of error movements is lacking in the mouse. Our wide-field imaging approach suggests that the widespread neural activity observed during successful RtGs is not generic to movement execution but rather the success of the completed goal-directed action.

There are some aspects that need to be considered when interpreting our results. The one-photon, wide-field calcium imaging approach is sensitive to light scattering potentially

leading to artifacts in the signals extracted from the cortical areas, which could increase the risk of erroneously treating an area as movement-associated (Yang and Yuste, 2017). Such possibility is reduced by the evidence that areas even in close proximity (e.g., the barrel fields vs the upper limb portion of the somatosensory cortex) do not display the same levels of activity (Fig. 4*A*). We concede that the number of neocortical clusters emerging during movement could be influenced by the parcellation of the neocortex, which may introduce spurious segregations beyond those that are physiologically present. Importantly, the overlap between the results obtained from the seed-pixel analysis and the CCM supports the existence of at least four distinct neocortical networks during voluntary motor control. The analyzed neural activity is inferred from the fluctuations of fluorescence intensity throughout time, a signal composed also by non-neuronal sources, notoriously of hemodynamic origin, which represents another artifact that needs to be taken into account (Ma et al., 2016a,b). However, the hemodynamic component of the signal has a much slower rise and decay time with respect to the neuronal signal. This temporal feature of the hemodynamic component of the *GCaMP6f* signal reduces its contribution relative to the results reported here (Scott et al., 2018). In addition, our control experiments on *GFP* mice allowed us to obtain signal components that were exclusive for GCaMP mice thus further mitigating the contribution of non-neuronal signals in our results.

The transgenic line used here reports variation in the activity of excitatory neurons only, leaving the question open as to what is the role played by other neural populations, considering, for instance, that GABAergic neurons in the primary motor cortex signal the initiation of voluntary reaching movements (Estebanez et al., 2017).

The temporal kinetics (50 ms rise time and 150 ms decay time) intrinsic to the optical probe used here (*GCaMP6f*) (Chen et al., 2013; Dana et al., 2014) entails that the neural dynamics faster than 50 ms associated with RtG were not investigated in the present study. Moreover, because of the indicator decay time, it is hard to disentangle events that occur within a time window of 150 ms. This is also the reason why we do not extend our analysis past the peak in the calcium wave for the correlation analysis. Finally, the activity patterns observed here refer mostly to relatively slow ($<$13 Hz) cortical communication schemes; nonetheless, neural activity in the lower frequency range (including frequencies $<$4 Hz) encodes several parameters of movement kinematics (Bansal et al., 2011). The adaptation for such tasks for head-fixed mice is more recent (Guo et al., 2015); and recently, the work of the same group revealed how input from the thalamus drives activity in the primary motor cortex and RtG movement (Sauerbrei et al., 2020).

To overcome the temporal constraints associated with calcium imaging, a crucial step forward will be represented by the adoption of genetically encoded voltage indicators for the study of neocortex-wide dynamics during skilled movements, as very recent technological advances offer sufficiently stable and bright signal-to-noise ratio for *in vivo* applications (Abdelfattah et al., 2019; Adam et al., 2019; Villette et al., 2019). Even considering such limitations, our findings remain unexpected and provide experimental evidence to put into question some dogmas of the classical literature in motor control (Omrani et al., 2017), at least when investigating the modus operandi of the rodent neocortex. The present neocortex-wide characterization of the neural activity patterns associated with RtGs is a step toward all-optical interrogation of neural circuits associated with this behavior.

In conclusion, our investigation identified a global network of neocortical areas beyond those previously known to be associated with goal-directed arm movements and suggest that the operating mode of the mouse neocortex underlying unilateral goal-directed movements involves distant communication across both hemispheres, whereas the encoding of movement parameters occurs locally, and, in the context of our investigations, mostly in the sensorimotor areas.

References

Abdelfattah AS, Kawashima T, Singh A, Novak O, Liu H, Shuai Y, Huang YC, Campagnola L, Seeman SC, Yu J, Zheng J, Grimm JB, Patel R, Friedrich J, Mensh BD, Paninski L, Macklin JJ, Murphy GJ, Podgorski K, Lin BJ, et al. (2019) Bright and photostable chemigenetic indicators for extended in vivo voltage imaging. Science 365:699–704.

Adam Y, Kim JJ, Lou S, Zhao Y, Xie ME, Brinks D, Wu H, Mostajo-Radji MA, Kheifets S, Parot V, Chettih S, Williams KJ, Gmeiner B, Farhi SL, Madisen L, Buchanan EK, Kinsella I, Zhou D, Paninski L, Harvey CD, et al. (2019) Voltage imaging and optogenetics reveal behaviour-dependent changes in hippocampal dynamics. Nature 569:413–417.

Allen WE, Kauvar IV, Chen MZ, Richman EB, Yang SJ, Chan K, Gradinaru V, Deverman BE, Luo L, Deisseroth K (2017) Global representations of goal-directed behavior in distinct cell types of mouse neocortex. Neuron 94:891–907.e6.

Allegra Mascaro AL, Conti E, Lai S, Spalletti C, Alia C, Panarese A, Scaglione A, Sacconi L, Micera S, Caleo M, Pavone FS (2019) Combined Rehabilitation Promotes the Recovery of Structural and Functional Features of Healthy Neuronal Networks after Stroke. Cell Reports 28:3474–3485.e6.

Bansal AK, Vargas-Irwin CE, Truccolo W, Donoghue JP (2011) Relationships among low-frequency local field potentials, spiking activity, and three-dimensional reach and grasp kinematics in primary motor and ventral premotor cortices. J Neurophysiol 105:1603–1619.

Barthas F, Kwan AC (2017) Secondary motor cortex: where "sensory" meets "motor" in the rodent frontal cortex. Trends Neurosci 40:181–193.

Battaglia-Mayer A, Caminiti R (2019) Corticocortical systems underlying high-order motor control. J Neurosci 39:4404–4421.

Bayne T, Brainard D, Byrne RW, Chittka L, Clayton N, Heyes C, Mather J, Ölveczky B, Shadlen M, Suddendorf T, Webb B (2019) What is cognition? Curr Biol 29:R608–R615.

Bollu T, Whitehead SC, Prasad N, Walker J, Shyamkumar N, Subramaniam R, Kardon B, Cohen I, Goldberg JH (2019) Automated home cage training of mice in a hold-still center-out reach task. J Neurophysiol 121:500–512.

Bundy DT, Leuthardt EC (2019) The cortical physiology of ipsilateral limb movements. Trends Neurosci 42:825–839.

Bundy DT, Szrama N, Pahwa M, Leuthardt EC (2018) Unilateral, 3D arm movement kinematics are encoded in ipsilateral human cortex. J Neurosci 38:10042–10056.

Chen TW, Wardill TJ, Sun Y, Pulver SR, Renninger SL, Baohan A, Schreiter ER, Kerr RA, Orger MB, Jayaraman V, Looger LL, Svoboda K, Kim DS (2013) Ultrasensitive fluorescent proteins for imaging neuronal activity. Nature 499:295–300.

Chen TW, Li N, Daie K, Svoboda K (2017) A map of anticipatory activity in mouse motor cortex. Neuron 94:866–879.e4.

Churchland MM, Cunningham JP, Kaufman MT, Foster JD, Nuyujukian P, Ryu SI, Shenoy KV (2012) Neural population dynamics during reaching. Nature 487:51–56.

Clancy KB, Orsolic I, Mrsic-Flogel TD (2019) Locomotion-dependent remapping of distributed cortical networks. Nat Neurosci 22:778–786.

Cohen JR, D'Esposito M (2016) The segregation and integration of distinct brain networks and their relationship to cognition. J Neurosci 36:12083–12094.

Czajkowski R, Jayaprakash B, Wiltgen B, Rogerson T, Guzman-Karlsson MC, Barth AL, Trachtenberg JT, Silva AJ (2014) Encoding and storage of spatial information in the retrosplenial cortex. Proc Natl Acad Sci USA 111:8661–8666.

Dana H, Chen TW, Hu A, Shields BC, Guo C, Looger LL, Kim DS, Svoboda K (2014) Thy1-GCaMP6 transgenic mice for neuronal population imaging in vivo. PLoS One 9:e108697.

Diedrichsen J, Hashambhoy Y, Rane T, Shadmehr R (2005) Neural correlates of reach errors. J Neurosci 25:9919–9931.
Ebina T, Masamizu Y, Tanaka YR, Watakabe A, Hirakawa R, Hirayama Y, Hira R, Terada SI, Koketsu D, Hikosaka K, Mizukami H, Nambu A, Sasaki E, Yamamori T, Matsuzaki M (2018) Two-photon imaging of neuronal activity in motor cortex of marmosets during upper-limb movement tasks. Nat Commun 9:1879.
Estebanez L, Hoffmann D, Voigt BC, Poulet JF (2017) Parvalbumin-expressing GABAergic neurons in primary motor cortex signal reaching. Cell Rep 20:308–318.
Evarts EV (1968) Relation of pyramidal tract activity to force exerted during voluntary movement. J Neurophysiol 31:14–27.
Galinanes GL, Bonardi C, Huber D (2018) Directional reaching for water as a cortex-dependent behavioral framework for mice. Cell Rep 22:2767–2783.
Georgopoulos AP, Kalaska JF, Caminiti R, Massey JT (1982) On the relations between the direction of two-dimensional arm movements and cell discharge in primate motor cortex. J Neurosci 2:1527–1537.
Goard MJ, Pho GN, Woodson J, Sur M (2016) Distinct roles of visual, parietal, and frontal motor cortices in memory-guided sensorimotor decisions. Elife 5:e13764.
Graziano MS, Taylor CS, Moore T (2002) Complex movements evoked by microstimulation of precentral cortex. Neuron 34:841–851.
Guo JZ, Graves AR, Guo WW, Zheng J, Lee A, Rodriguez-Gonzalez J, Li N, Macklin JJ, Phillips JW, Mensh BD, Branson K, Hantman AW (2015) Cortex commands the performance of skilled movement. Elife 4:e10774.
Hakon J, Quattromani MJ, Sjölund C, Tomasevic G, Carey L, Lee JM, Ruscher K, Wieloch T, Bauer AQ (2018) Multisensory stimulation improves functional recovery and resting-state functional connectivity in the mouse brain after stroke. Neuroimage Clin 17:717–730.
Heming EA, Cross KP, Takei T, Cook DJ, Scott SH (2019) Independent representations of ipsilateral and contralateral limbs in primary motor cortex. eLife 8:e48190.
Hira R, Ohkubo F, Tanaka YR, Masamizu Y, Augustine GJ, Kasai H, Matsuzaki M (2013) In vivo optogenetic tracing of functional corticocortical connections between motor forelimb areas. Front Neural Circuits 7:55.
Hwang EJ, Dahlen JE, Hu YY, Aguilar K, Yu B, Mukundan M, Mitani A, Komiyama T (2019) Disengagement of motor cortex from movement control during long-term learning. Sci Adv 5:eaay0001.
Kyriakatos A, Sadashivaiah V, Zhang Y, Motta A, Auffret M, Petersen CC (2017) Voltage-sensitive dye imaging of mouse neocortex during a whisker detection task. Neurophotonics 4:031204.
Lai S, Panarese A, Spalletti C, Alia C, Ghionzoli A, Caleo M, Micera S (2015) Quantitative kinematic characterization of reaching impairments in mice after a stroke. Neurorehabil Neural Repair 29:382–392.
Li C, Chan DC, Yang X, Ke Y, Yung WH (2019) Prediction of forelimb reach results from motor cortex activities based on calcium imaging and deep learning. Front Cell Neurosci 13:88.
Li N, Daie K, Svoboda K, Druckmann S (2016) Robust neuronal dynamics in premotor cortex during motor planning. Nature 532:459–464.
Ma Y, Shaik MA, Kim SH, Kozberg MG, Thibodeaux DN, Zhao HT, Yu H, Hillman EM (2016a) Wide-field optical mapping of neural activity and brain haemodynamics: considerations and novel approaches. Philos Trans R Soc Lond B Biol Sci 371:20150360.
Ma Y, Shaik MA, Kozberg MG, Kim SH, Portes JP, Timerman D, Hillman EM (2016b) Resting-state hemodynamics are spatiotemporally coupled to synchronized and symmetric neural activity in excitatory neurons. Proc Natl Acad Sci USA 113:E8463–E8471.
Makino H, Ren C, Liu H, Kim AN, Kondapaneni N, Liu X, Kuzum D, Komiyama T (2017) Transformation of cortex-wide emergent properties during motor learning. Neuron 94:880–890.e8.
Montagni E, Resta F, Conti E, Scaglione A, Pasquini M, Micera S, Allegra Mascaro AL, Pavone FS (2019) Wide-field imaging of cortical neuronal activity with red-shifted functional indicators during motor task execution. J Phys D: Appl Phys 52:074001.
Morandell K, Huber D (2017) The role of forelimb motor cortex areas in goal directed action in mice. Sci Rep 7:15759.
Musall S, Kaufman MT, Juavinett AL, Gluf S, Churchland AK (2019) Single-trial neural dynamics are dominated by richly varied movements. Nat Neurosci 22:1677–1686.
Mutha PK, Haaland KY, Sainburg RL (2013) Rethinking motor lateralization: specialized but complementary mechanisms for motor control of each arm. PLoS One 8:e58582.
Ölveczky BP (2011) Motoring ahead with rodents. Curr Opin Neurobiol 21:571–578.
Omrani M, Kaufman MT, Hatsopoulos NG, Cheney PD (2017) Perspectives on classical controversies about the motor cortex. J Neurophysiol 118:1828–1848.
Peters AJ, Chen SX, Komiyama T (2014) Emergence of reproducible spatiotemporal activity during motor learning. Nature 510:263–267.
Pnevmatikakis EA, Soudry D, Gao Y, Machado TA, Merel J, Pfau D, Reardon T, Mu Y, Lacefield C, Yang W, Ahrens M, Bruno R, Jessell TM, Peterka DS, Yuste R, Paninski L (2016) Simultaneous denoising, deconvolution, and demixing of calcium imaging data. Neuron 89:285–299.
Prsa M, Galinanes GL, Huber D (2017) Rapid integration of artificial sensory feedback during operant conditioning of motor cortex neurons. Neuron 93:929–939.e6.
Ren C, Komiyama T (2021) Characterizing Cortex-Wide Dynamics with Wide-Field Calcium Imaging. J Neurosci 41:4160–4168.
Salkoff DB, Zagha E, McCarthy E, McCormick DA (2020) Movement and performance explain widespread cortical activity in a visual detection task. Cereb Cortex 30:421–437.
Sancataldo G, Silvestri L, Allegra Mascaro AL, Sacconi L, Pavone FS (2019) Advanced fluorescence microscopy for in vivo imaging of neuronal activity. Optica 6:758–765.
Sauerbrei BA, Guo JZ, Cohen JD, Mischiati M, Guo W, Kabra M, Verma N, Mensh B, Branson K, Hantman AW (2020) Cortical pattern generation during dexterous movement is input-driven. Nature 577:386–391.
Saxena S, Kinsella I, Musall S, Kim SH, Meszaros J, Thibodeaux DN, Kim C, Cunningham J, Hillman EM, Churchland A, Paninski L (2020) Localized semi-nonnegative matrix factorization (LocaNMF) of widefield calcium imaging data. PLoS Comput Biol 16:e1007791.
Schaffer JE, Sainburg RL (2017) Interlimb differences in coordination of unsupported reaching movements. Neuroscience 350:54–64.
Scott BB, Thiberge SY, Guo C, Tervo DG, Brody CD, Karpova AY, Tank DW (2018) Imaging cortical dynamics in GCaMP transgenic rats with a head-mounted widefield macroscope. Neuron 100:1045–1058.e5.
Soma S, Yoshida J, Kato S, Takahashi Y, Nonomura S, Sugimura YK, Rios A, Kawabata M, Kobayashi K, Kato F, Sakai Y, Isomura Y (2019) Ipsilateral-dominant control of limb movements in rodent posterior parietal cortex. J Neurosci 39:485–502.
Stringer C, Pachitariu M, Steinmetz N, Reddy CB, Carandini M, Harris KD (2019) Spontaneous behaviors drive multidimensional, brainwide activity. Science 364:255.
Tennant KA, Adkins DL, Donlan NA, Asay AL, Thomas N, Kleim JA, Jones TA (2011) The organization of the forelimb representation of the C57BL/6 mouse motor cortex as defined by intracortical microstimulation and cytoarchitecture. Cereb Cortex 21:865–876.
Vanni MP, Chan AW, Balbi M, Silasi G, Murphy TH (2017) Mesoscale mapping of mouse cortex reveals frequency-dependent cycling between distinct macroscale functional modules. J Neurosci 37:7513–7533.
Villette V, Chavarha M, Dimov IK, Bradley J, Pradhan L, Mathieu B, Evans SW, Chamberland S, Shi D, Yang R, Kim BB, Ayon A, Jalil A, St-Pierre F, Schnitzer MJ, Bi G, Toth K, Ding J, Dieudonné S, Lin MZ (2019) Ultrafast two-photon imaging of a high-gain voltage indicator in awake behaving mice. Cell 179:1590–1608.e23.
Wang X, Liu Y, Li X, Zhang Z, Yang H, Zhang Y, Williams PR, Alwahab NS, Kapur K, Yu B, Zhang Y, Chen M, Ding H, Gerfen CR, Wang KH, He Z (2017) Deconstruction of corticospinal circuits for goal-directed motor skills. Cell 171:440–455.e14.
Ward JH Jr (1963) Hierarchical grouping to optimize an objective function. J Am Statist Assoc 58:236–244.
Wekselblatt JB, Flister ED, Piscopo DM, Niell CM (2016) Large-scale imaging of cortical dynamics during sensory perception and behavior. J Neurophysiol 115:2852–2866.
Whishaw IQ, Faraji J, Kuntz J, Mirza Agha B, Patel M, Metz GA, Mohajerani MH (2017) Organization of the reach and grasp in head-fixed vs freely-moving mice provides support for multiple motor channel theory of neocortical organization. Exp Brain Res 235:1919–1932.
Yang W, Yuste R (2017) In vivo imaging of neural activity. Nat Methods 14:349–359.